

SENIOR THESIS

CHARGE COLLECTION IN 3D SILICON SENSORS

Name Adam Yañez
Advisors Sally Seidel and Martin Hoferkamp
School University of New Mexico
Department Physics and Astronomy
Email ayanez2@unm.edu
Date May 13, 2021



THE UNIVERSITY OF
NEW MEXICO.

Abstract

Silicon pixel sensors of the 3D configuration have been studied to evaluate their ability to multiply charge, both before and after their exposure to radiation. These are being developed for accelerators like the Large Hadron Collider at CERN, which are used to study elementary particles and search for new physics beyond the Standard Model. The radiation produced in the collisions also damages the sensors used to track the particles. The Large Hadron Collider is due to be upgraded by the end of the decade to increase the luminosity by a factor of ten. Scientists are searching for ways to make the sensors used in the detectors more resistant to the damage sustained from normal operations. One proposed technology is 3D silicon sensors. Here, the efficiency of small-pitch 3D silicon sensors is reported following measurements of charge collection after exposure to different fluences of proton radiation. A 3D silicon sensor with a surface geometry of $25 \times 25 \mu\text{m}^2$ under a proton fluence of $3.0 \times 10^{16} \text{ n}_{\text{eq}}/\text{cm}^2$ allows for a charge multiplication gain of up to 2.0 ± 0.2 before electrical breakdown onsets. The results provide proof that small-pitch 3D silicon sensors will multiply charge at operating voltages even under the increased luminosity conditions of the High-Luminosity upgrade to the Large Hadron Collider.

Contents

Abstract	ii
1 Introduction	1
1.1 Large Hadron Collider	1
1.2 Semiconductors	3
1.3 PN Junction	5
1.4 Radiation Damage	6
2 Sensors	7
2.1 Description of 3D sensors	7
2.2 Depletion and Breakdown Voltages	8
2.3 Signal Charge Creation and Collection	9
2.4 Charge Multiplication	9
2.5 Readout Electronics	11
2.6 Sources of Noise	11
3 Setup	13
3.1 Setup for Measurement of Breakdown Voltage	13
3.2 Setup for Measurement of Depletion Voltage	14
3.3 Setup for Measurement of Charge Collection Efficiency	15
4 Results	19
5 Conclusion	22
References	24
Appendix	25

1. Introduction

1.1 Large Hadron Collider

The Large Hadron Collider (LHC) at CERN in Geneva, Switzerland is the largest and highest energy particle collider in the world. The LHC ring is located 100 m underground and is 27 km in circumference. It is designed to accelerate hadrons, primarily protons, at over 99% the speed of light and guide them to collide at one of four interaction points. Sophisticated detectors are located at each of the interaction points. These detectors were designed to carry out specific measurements for experiments.

The path the protons follow starts at a linear accelerator, followed by successively larger and larger rings. Fig. 1.1 shows the CERN complex with the names of the rings and the dates of their construction. Superconducting magnets are used to accelerate the protons around the rings. The protons take several turns at each ring to pick up energy. At the SPS (Super Proton Synchrotron) ring, which is the ring before the LHC ring, the proton beam is split in two and the two beams enter the LHC ring in opposite directions. The LHC ring continues to accelerate the protons until they reach a kinetic energy of 6.5 TeV. Therefore, when the protons collide, they have a total energy of 13 TeV.

The protons are accelerated through alternating electric fields. As a consequence, the protons are grouped in bunches as they accelerate around the rings [16]. They are spaced so that there are 25 ns between crossings. Events in which more than one collision takes place during a beam crossing produce multiple events atop the one of interest - these are called pileup events [14]. There are about 33 simultaneous collisions per crossing. Upon collision, the protons are annihilated and produce outgoing elementary particles. These particles pass through the detectors, which can measure the particles' trajectories, momenta, and energies.

The amount of data generated by the collisions is immense, with hundreds of petabytes of data recorded every year. Triggers at the hardware and software level filter out the majority of data from collisions, with only one collision in one million being of interest. The data are stored on-site at CERN and are redistributed to several data centers around the world for analysis and simulation.

The CERN accelerator complex *Complexe des accélérateurs du CERN*

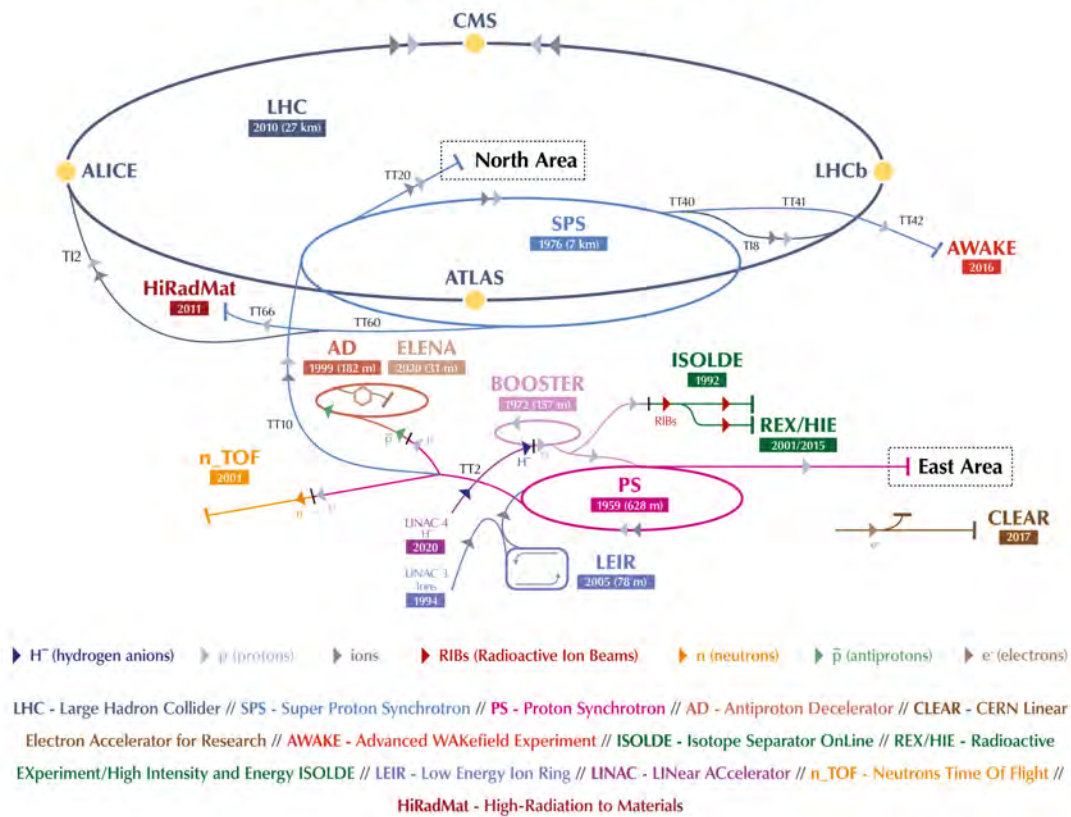


Figure 1.1: CERN Complex. Some major components are labeled with their name and the year of their construction. The image is reproduced from source [5].

Of the four detectors at the LHC, the one with which we work at the University of New Mexico (UNM) is the ATLAS detector. It is a cylinder that measures 25 m in diameter by 44 m in length and surrounds the interaction point with hundreds of square meters of detectors. Fig. 1.2 shows an ATLAS detector cutaway with the different layers of the detector visible. The component closest to the interaction point is called the pixel detector. Its purpose is to determine the location of secondary vertices which occur when a particle decays after the initial collision. The ATLAS and the CMS detectors are general purpose detectors; the other two main detectors on the LHC ring are ALICE (primarily intended for study of heavy ion collisions) and LHCb (primarily intended for study of events involving b-quarks). The focus of ATLAS is on collecting precise measurements of the Higgs boson as well as the search for new physics beyond the Standard Model.

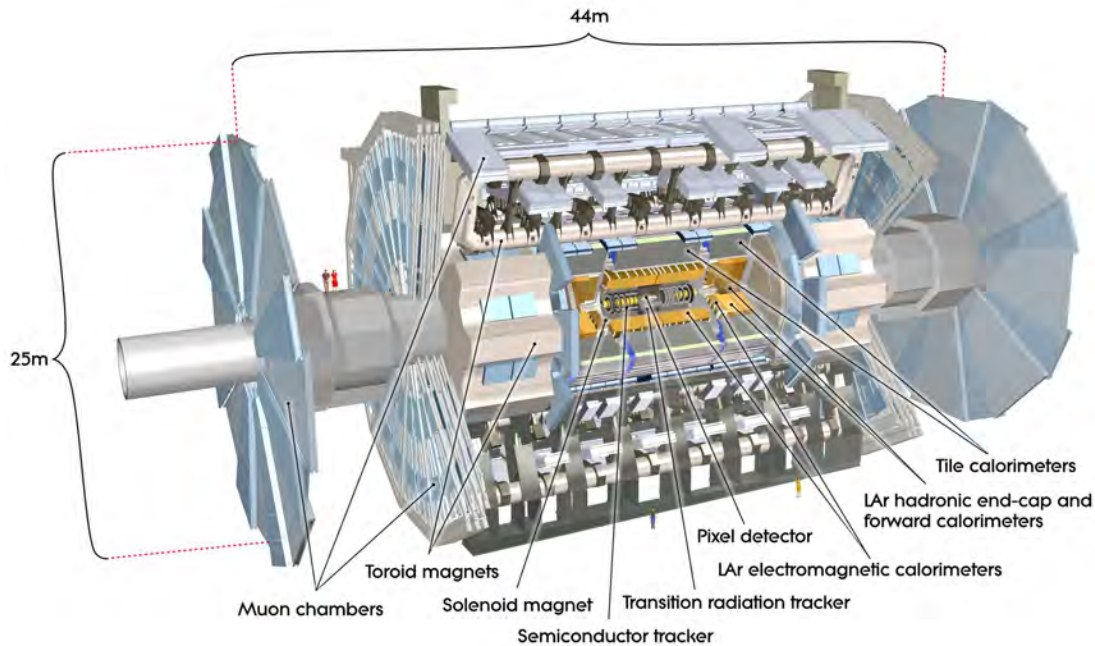


Figure 1.2: ATLAS Detector. This cut-away view shows the dimensions and labels for some of the components. The image is reproduced from source [9].

The plan for the LHC for the next decade is to increase the number of collisions by a factor of 10. The High Luminosity upgrade to the LHC (HL-LHC) will involve upgrading the superconducting magnets, beam collimators, and RF cavities used to accelerate beams. The increased luminosity will especially affect the pixel detector, as more collisions will create more particles which will increase the amount of radiation damage sustained by the detector. 3D sensors may be utilized there to withstand the increased damage and are being studied around the world under the increased luminosity conditions expected in the HL-LHC.

1.2 Semiconductors

Semiconductor devices are used in a variety of applications today. In particle physics, they are used to track particles' trajectories as the particles pass through the semiconductor bulk. The electrons in a semiconductor form energy bands called the valence and conduction bands. This is due to the interaction of electrons of neighboring atoms and the Pauli exclusion principle. As atoms are brought closer together, their valence electrons begin to interact. Since no two electrons can be in the same quantum state, the electrons form allowed and forbidden energy bands. The width of the forbidden region between energy bands is called the bandgap energy.

An electron must acquire at least the bandgap energy for it to move from the valence band to the conduction band. When this happens, it is free to move around the lattice as it is only loosely bound to its parent atom. In a pure silicon crystal, there are no allowed energy states in the forbidden region. Adding impurities to the crystal introduces intermediate energy states in the forbidden region. These intermediate energy states allow electrons to move into the conduction band with less energy.

Charge carriers in a semiconductor can be either an electron that has moved from the valence band to the conduction band, or holes which are the vacated states in the valence band that are left when an electron migrates to the conduction band. A hole can move through a semiconductor when an electron from a neighboring atom moves into the hole and leaves behind its own vacancy. The movement of charge carriers generates a current.

A semiconductor consists of a bulk substrate with one or more dopant elements injected into the lattice. Semiconductors have a conductivity between those of metals and insulators. This property allows them to behave as insulators under certain conditions and conductors in others.

The bulk substrate which our sensors use is silicon. Other group IV elements can be used, as can compound substrates consisting of two or more elements. To create a silicon substrate, elemental silicon is heated to its melting point. A crystal seed is placed into the liquid silicon. The silicon atoms start to aggregate on the crystal seed and repeat the pattern as they aggregate. The pattern desired is a single-crystal diamond or tetrahedral lattice. The atoms in the lattice are connected to four neighbors. The four valence electrons in the silicon atom are responsible for this pattern. The silicon atoms form covalent bonds with the four nearest neighbors, giving the atoms inside the lattice a full valence shell of electrons.

The substrate crystal can be sliced to form wafers, which will be ready to accept dopant atoms. These dopant atoms form impurities in the silicon substrate and change the conductive properties of the material. The impurity type desired is a substitution. This means that the dopant atom replaces a silicon atom in the lattice. Typically, dopant atoms are either group III or group V elements, with boron and phosphorus respectively being the most common. A boron atom has one fewer electron in its valence shell than a silicon atom. A phosphorus atom has one more electron in its valence shell than a silicon atom.

A boron dopant atom has three valence electrons. When it is injected into the silicon substrate, those three valence electrons will form covalent bonds with three silicon atoms. The fourth silicon atom will not have a covalent bond, but will be able to accept an electron from neighboring atoms. For these reasons, a boron atom is called an acceptor atom and a semiconductor doped with boron is a p-type semiconductor.

A phosphorus atom has five valence electrons. In a silicon substrate, four of the five valence electrons will form covalent bonds with the four nearest neighboring silicon atoms. The extra valence electron is loosely bound to the phosphorus atom. It is so loosely bound that it can travel, or diffuse, and is not confined to the range of a specific nucleus. Thus, a phosphorus atom is called a donor or n-type dopant.

1.3 PN Junction

A pn junction is an interface between p-type and n-type semiconductors within a single crystal. Through stochastic motion, electrons from the n region will diffuse to the p region. The electrons will fill in the holes in the p region and will create a net negative charge. The absence of electrons in the n region will leave that region positively charged. This creates an electric field that grows in magnitude as more electrons diffuse to the p region. The electric field will grow until it reaches equilibrium and counteracts the diffusion of electrons into the p region.

As the electrons travel from the n to the p region, the area is depleted of free charge carriers. The area with no free charge carriers is called the depletion region. The width of the depletion region can be changed by applying a potential difference across the pn junction. To decrease the width of the depletion region, a bias voltage with a higher potential on the p side and lower potential on the n side can be applied. This is called a forward bias voltage. The semiconductor will behave as a conductor as charge carriers will be free to move through the pn junction to create a current.

To increase the width of the depletion region, a bias voltage with a higher potential on the n side and lower potential on the p side can be applied. This is called a reverse bias voltage. The potential difference can be increased until the entire n-type region is fully depleted of charge carriers. At this point, the semiconductor behaves as an insulator as there are no free charge carriers to create a current. Thermal excitation of electrons can still contribute to a small current called leakage current. Fig. 1.3 shows how the pn junction is changed with forward and reverse bias voltages applied.

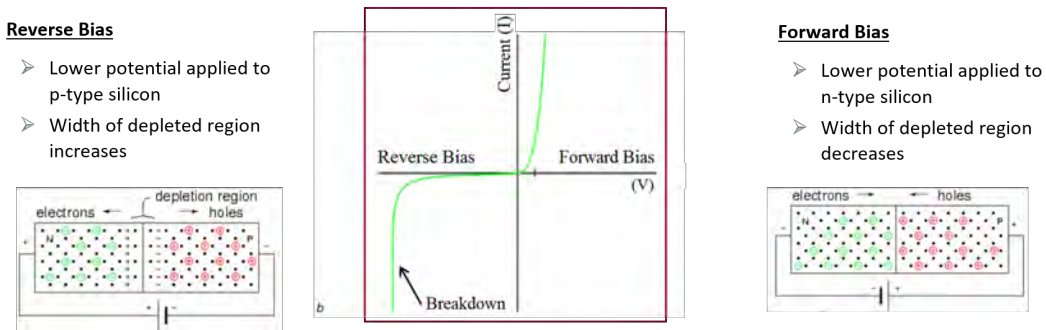


Figure 1.3: Current versus voltage graph for a pn junction (center). As a reverse bias voltage is applied, the depletion region grows (left). If a forward bias voltage is applied, a current is induced (right).

Further increasing the reverse bias voltage will create a strong electric field. At the pn junction, the energy bandgap between the valence band in the p region and conduction band in the n region will be small enough that electrons will be able to tunnel through the gap. This is called the Zener breakdown [7]. Another consequence of the high electric field is that electrons will gain enough energy to collide with and ionize other electrons as they travel along the electric field. This is called avalanche breakdown [7]. The semiconductor will become conductive in either case and will allow current to pass through.

1.4 Radiation Damage

Silicon semiconductors are prone to two types of damage due to radiation: displacement damage and ionization damage. Displacement damage is caused by radiation which imparts its energy to atoms in the lattice and displaces them. These displacements form electron energy states between the conduction and valence bands. Electrons that enter these states leave behind vacancies that attract electrons and increase the current at a given bias voltage. This contributes to leakage current [6]. Displacements can also trap electrons from the conduction band that form a signal current. Electrons in the conduction band fall into one of these mid-gap states and are released after a time causing signal delay [6].

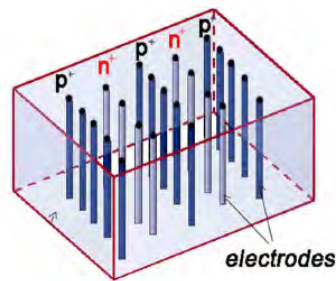
Ionization damage happens at the surface of semiconductor detectors. A layer of silicon dioxide at the surface of detectors regulates the electric field at the surface and keeps charge carriers from becoming trapped in the dangling bonds at the surface of the bulk crystal lattice [13]. When radiation is incident on this layer, it may ionize the silicon dioxide. The charge carriers generated this way become trapped at the interface between the silicon dioxide and the sensor bulk. The trapped charges may then cause breakdown to occur at lower voltages because of the generated surface current [3].

To mitigate charge trapping in the bulk, 3D silicon sensors are being fabricated with their electrodes perpendicular to the sensor surface. Their main advantage over planar sensors, which have the electrodes on opposing surfaces of the sensor, is that the distance between electrodes is independent of the thickness of the sensor. Reducing the distance between electrodes reduces the probability of charge carriers becoming trapped. The shorter distance also allows for full depletion and an increase in electric field magnitude at lower voltages. A stronger electric field increases the probability of charge multiplication due to avalanche breakdown. The details of 3D sensors are discussed in the following sections.

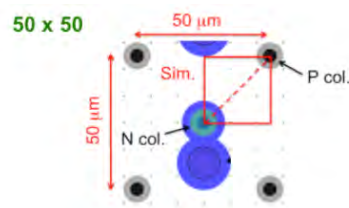
2. Sensors

2.1 Description of 3D sensors

The sensors used in this study are 3D silicon sensors fabricated in 2018 by FBK in Trento, Italy. They feature an n-type bulk with highly-doped n^+ and p^+ type columnar electrodes which are $5\ \mu\text{m}$ in diameter and penetrate the sensor bulk. The sensors are $120\ \mu\text{m}$ thick. Fig. 2.1 shows how the electrode columns are arranged and how cell size is determined.



(a) Sensor profile showing electrode columns. Image reproduced from source [18].



(b) Sample cell diagram. Image reproduced from source [1].

Figure 2.1: These drawings show details of 3D silicon sensors. The left image shows how electrode columns are arranged in the bulk of the sensor. On the right is a drawing of a cell with dimensions of $50 \times 50\ \mu\text{m}^2$.

The p^+ type electrodes are connected at the back side of the sensor to a conductive aluminum surface. The n^+ type electrodes are connected to each other with either metal or p-doped polysilicon traces. The traces all connect to a set of contact pads on the top surface of the sensors. The contact pads allow measurements of leakage current and capacitance for the whole sensor. Sensors used in particle accelerators would not have these traces. Instead, they would be separated into cells with either one or two n^+ type electrodes connected to their own set of readout electronics. This extra structure is included in the sensors involved in this study to simplify the process of measuring their bulk electrical characteristics in the absence of an amplifier.

A single cell consists of a number of p^+ electrodes surrounding one or two n^+ electrodes. For cells with one n^+ electrode, there are four surrounding p^+ electrodes. These are designated with a 1E after their name. For cells with two n^+ electrodes, there are six surrounding p^+ electrodes. These sensors are designated with a 2E after their name. Adjacent cells share p^+ electrodes. The cells are arranged in regular rectangular patterns.

Cell sizes are determined by the distance between the p^+ electrodes which surround the n^+ electrodes. The size of the cell is important because it determines the position resolution. The cell sizes are $25 \times 25 \mu\text{m}^2$ with one electrode per cell (1E), $50 \times 50 \mu\text{m}^2$ 1E, $25 \times 100 \mu\text{m}^2$ 1E, and $25 \times 100 \mu\text{m}^2$ 2E. Fig. 2.2 shows the surface features of the sensors described above. Two sensors with the same cell size are fabricated on one wafer with one version having metal traces and the other p-type polysilicon.

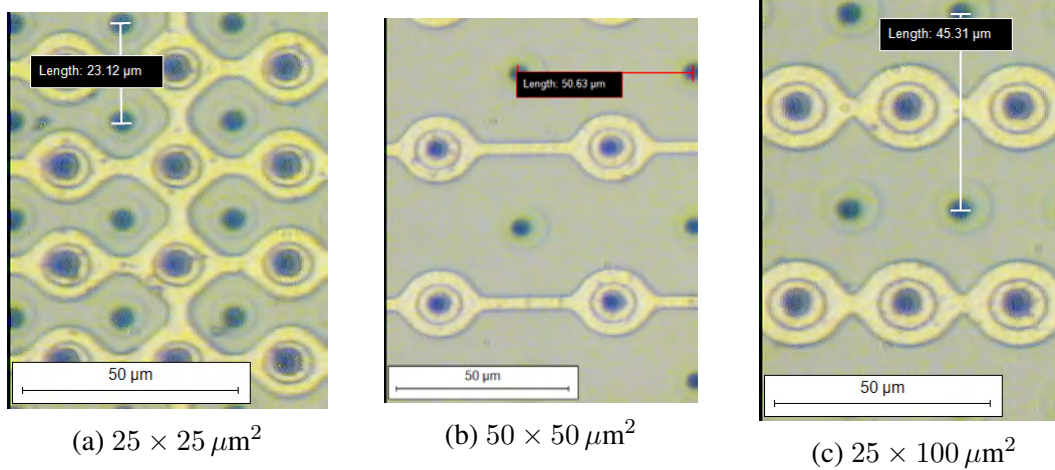


Figure 2.2: These photographs, taken at UNM, show a top-down view of the surface features of the sensors used. The black dots are tops of the electrodes

Sensors with all of these cell sizes were exposed to a range of proton fluences. Because sensors in particle colliders can be subjected to different types of radiation from charged and uncharged particles, the radiation received from an arbitrary particle is normalized to that of 1 MeV neutrons and abbreviated as n_{eq} [10]. The fluences used are $1.3 \times 10^{16} n_{\text{eq}}/\text{cm}^2$, $1.9 \times 10^{16} n_{\text{eq}}/\text{cm}^2$, and $3.0 \times 10^{16} n_{\text{eq}}/\text{cm}^2$. A control group with no exposure to radiation was also measured. The irradiation was conducted by UNM group members at the Los Alamos LANSCE 800 MeV proton beam. The effects of radiation damage persist and worsen even after the exposure has ended. For this reason the irradiated devices are stored at low temperature continuously from the time of radiation until the time of measurement, as this inhibits the reverse annealing process [10].

2.2 Depletion and Breakdown Voltages

The 3D silicon sensors operate between their depletion and breakdown voltages. Depletion and breakdown voltages must be known to determine the range of safe operating voltages. Depletion voltage is obtained by measuring capacitance in the sensors. Bulk capacitance for the entire sensor is measured between the n^+ and p^+ electrodes for a range of bias voltages. A plot of $1/C^2$ versus bias voltage is made, where C is the bulk capacitance. Starting at 0 V bias voltage, capacitance will decrease as the potential difference is increased and the sensor is depleted of charge carriers in the bulk between electrodes. Once the sensor is depleted, capacitance will stop decreasing and plateau. The points above and below the onset of the plateau are fitted to separate lines, and the intersection of the two lines determines the depletion voltage.

Breakdown voltage is determined by applying a reverse bias voltage to the sensors and measuring current. A reverse bias voltage will cause the semiconductor sensor to behave as an insulator, and only allow a small leakage current to pass through the sensor. The leakage current is caused by thermal excitation of electrons which drift towards the electrodes under the influence of the applied electric field. As bias voltage increases, the number of thermally excited electrons should remain the same, but the electrons will have a higher kinetic energy as they travel through the sensor towards the electrodes. If the bias voltage is further increased, the kinetic energy of the electrons will reach levels sufficient to ionize other atoms in the sensor, causing avalanche breakdown. This causes the current to increase sharply. The voltage at which this occurs is called breakdown voltage.

2.3 Signal Charge Creation and Collection

When a minimum ionizing particle passes through a silicon detector, it creates electron-hole (e-h) pairs by ionizing the atoms in the crystal. The electron-hole pairs are mostly confined in a tube of diameter of about $1\ \mu\text{m}$ around the track [8]. Under an electric field due to the reverse bias voltage applied across the electrodes, the electrons will drift to the n^+ electrodes and the holes will drift to the p^+ electrodes.

The drift velocity v is given by

$$v = \mu E$$

where μ is the mobility of the charge carriers under an electric field E . The mobility in silicon is $1450\ \text{cm}^2/\text{V}\cdot\text{s}$ for electrons and $480\ \text{cm}^2/\text{V}\cdot\text{s}$ for holes [8]. This means that electrons will travel to the n^+ electrodes three times faster than holes, which makes them the desired charge carrier to collect for signal. The moving charge carriers will induce a signal current as soon as they start drifting towards the electrodes. The signal current creation is complete once the charge carriers reach the electrodes.

A 1064 nm laser can be applied to the sensor to create electron-hole pairs. The infrared laser is able to penetrate the bulk of the sensor to stimulate the entire depth. Photons with an energy higher than the band gap energy of the silicon are able to create electron-hole pairs in the sensor [11]. The charge carriers created in this way contribute to the signal current.

2.4 Charge Multiplication

The process known as avalanche breakdown involves impact ionization of host atoms by energetic carriers. In pn junctions of interest for particle detectors, at least one side of the junction has low doping and can be fully depleted in normal operation before breakdown occurs. In a 3D detector designed for charge multiplication, the active volume of the detector is fully depleted.

Avalanche breakdown induces high charge flow in semiconductors that would normally show an insulating behavior (as in reverse bias conditions). An applied electric field can accelerate electrons (and holes to a lesser extent) in the junction so they achieve a large kinetic energy. When the accelerated electron impacts the semiconductor atoms, other free electron-hole pairs are formed. Both the original and the newly generated free electrons are again accelerated by the high electric field and subsequent impacts produce other electron-hole pairs. This phenomenon is known as impact ionization [15].

Impact ionization in silicon sensors begins when the internal electric field reaches about 180 kV/cm [17]. However, electric field levels of 200 – 300 kV/cm should be reached in order for impact ionization rates to become self-sustaining, that is greater than 10^3 cm^{-1} . The ionization rate describes how many electron-hole pairs can be generated per unit length by one electron via impact ionization. Fig. 2.3 shows the dependence of the ionization rate α_n of electrons on the electric field in silicon. Charge multiplication in 3D sensors relies on electric fields inside the sensor to be high enough to reach impact ionization.

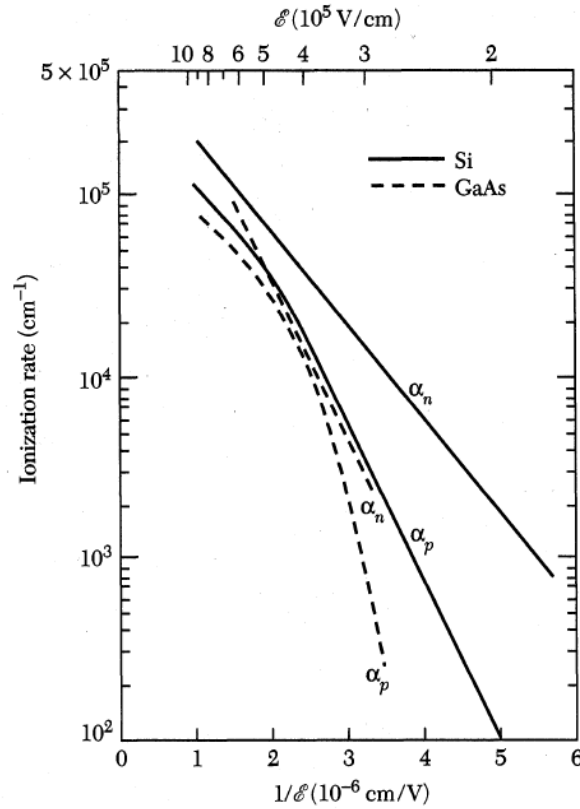


Figure 2.3: The ionization rates for electrons and holes are shown for silicon and gallium. The ionization rate of interest for this study is α_n for silicon. The image is reproduced from source [17].

2.5 Readout Electronics

To collect the signal charge from the detector, a charge sensitive amplifier (current integrator) configuration is used which integrates the detector charge Q_{det} onto the feedback capacitor C_f . The output signal V_O from the amplifier is given by

$$V_O = Q_{\text{det}}/C_f.$$

The shaping function is formed by high-pass and low-pass filters which shape the signal at the output of the preamplifier into a low-noise pulse where the peak value represents the integrated sensor charge. The digital pulse processor provides an improved filter compared to the traditional CR-RC analog method. Fig. 2.4 shows a circuit diagram for the readout electronics with the sensor included.

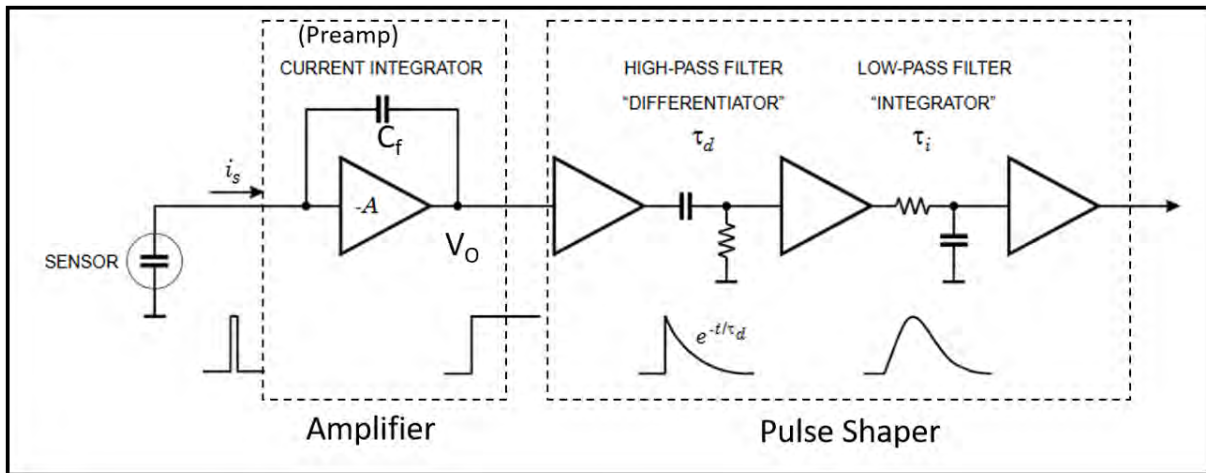


Figure 2.4: The circuit diagram for readout electronics with sensor. The image is reproduced from source [13].

2.6 Sources of Noise

The equivalent circuit for the noise analysis includes both current and voltage noise sources. The leakage current of a silicon detector fluctuates due to continuous electron emission statistics. This bias (leakage) current shot noise I_b is represented by a current noise generator in parallel with the detector. Fig. 2.5 shows a diagram of the sources of noise in the charge collection system. The statistical fluctuations in the charge measurement scale with the square root of the total number of recorded charges, so this noise contribution increases with the width of the shaped output pulse. Resistors exhibit noise due to the thermal velocity fluctuations of the charge carriers. Resistors shunting the input act as noise current sources and resistors in series with the input act as noise voltage sources. Since the bias resistor R_b effectively shunts the input it acts as a current generator and its noise current has the same effect as the shot noise current from the detector. The series resistor R_s acts as a voltage generator. The electronic noise of the amplifier is described fully by a combination of voltage and current sources at its input, shown as v_{na}^2 .

The large increase in bias current of highly irradiated sensors is the biggest source of noise in a charge collection system [12]. This can be mitigated by the use of a thermal chuck to cool the sensor from 25 °C to -20 °C. The leakage current at a reference temperature T_R (in kelvin) can be determined [4] from the leakage current at a measured temperature T_M scaled by a factor $R(T_M)$ using

$$I(T_R) = I(T_M) \times R(T_M)$$

where

$$R(T_M) = \left(\frac{T_R}{T_M}\right)^2 \exp\left(\frac{E_{\text{eff}}}{2k_B} \left[\frac{1}{T_R} - \frac{1}{T_M}\right]\right).$$

E_{eff} in silicon sensors has been measured as 1.21 eV after irradiation [4]. This relationship shows that reducing the temperature reduces the bias current by a factor of 2 for every 8 °C.

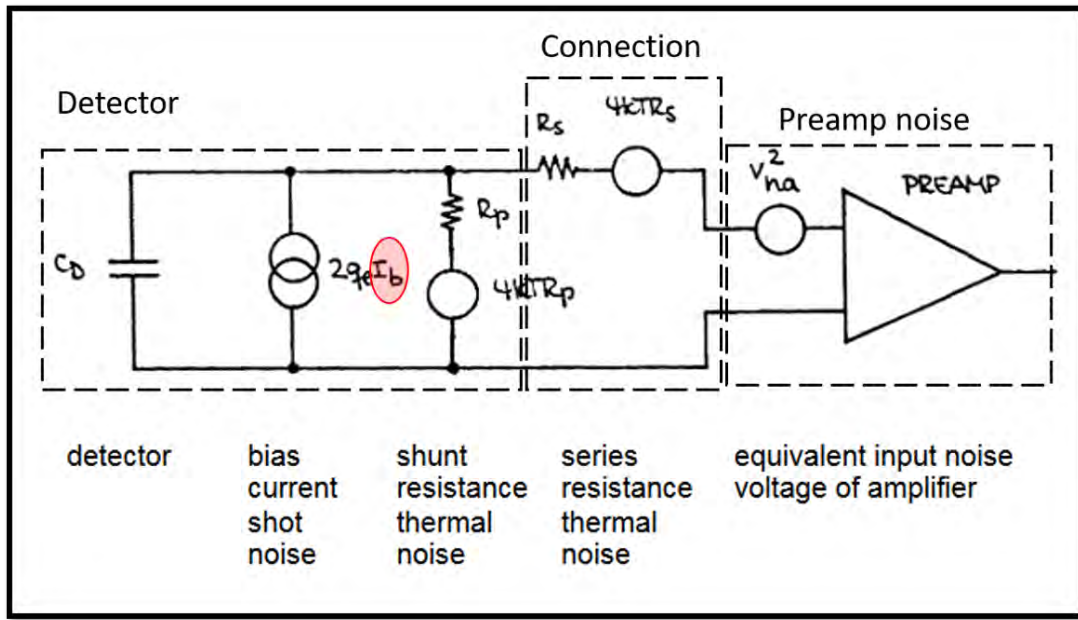


Figure 2.5: The sources of noise for the charge collection system. The red circle indicates the main contributor to noise in the system: the bias current shot noise. The image is reproduced from source [12].

3. Setup

3.1 Setup for Measurement of Breakdown Voltage

The sensors are sensitive to light, so they are enclosed along with the probe station in a light-tight enclosure during measurements. Fig. 3.1 shows the probe station inside the light-tight enclosure. The sensors are measured one at a time. Fig. 3.2 shows a schematic for the breakdown voltage measurements setup. A Keithley 237 high-voltage Sourcemeter is connected to the contact pads via a $0.6\ \mu\text{m}$ needle probe. The sensor chip is placed on a conductive surface connected to the ground of the Sourcemeter.

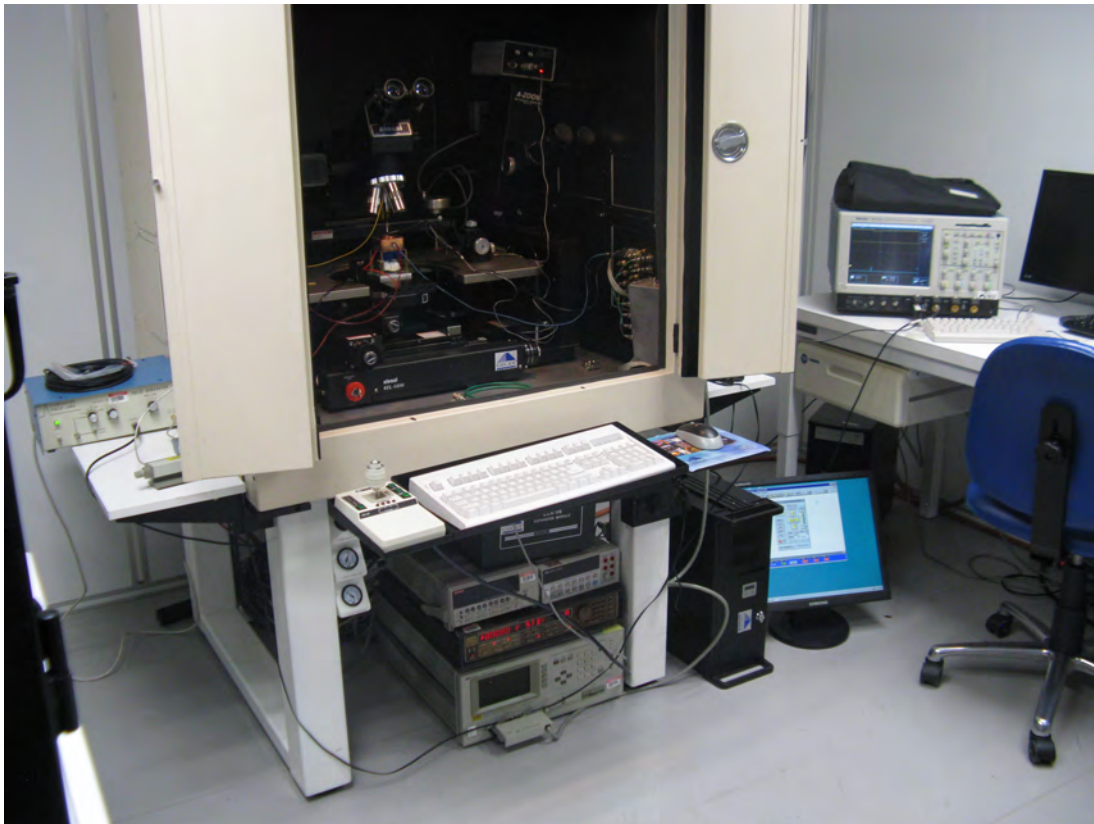


Figure 3.1: Photograph, taken at UNM, of the probe station inside the light-tight enclosure with the door open. Also shown in the picture are the power source and meters used to make measurements. The meters are connected to the computer on the desk to the right.

The sensors are cooled to $-20\text{ }^{\circ}\text{C}$. This is done to minimize the thermal excitation of electrons in the sensor which contribute to the increased leakage current. The setup for this measurement uses a Micromanipulator attached to a thermal chuck. A liquid coolant is used to remove waste heat from the thermal chuck. The Micromanipulator allows the chuck to be set to a constant temperature. To prevent condensation from forming on the sensor, nitrogen gas at room temperature is blown over the sensor.

A computer with LabVIEW controls the Sourcemeter and records the measurements. A reverse bias voltage is applied and swept from 0 to 200 V in 1 V increments. Three measurements of current are made at each step. Breakdown voltage is recorded when there is a sharp increase in current. Graphs for the breakdown voltages of the sensors used in this study can be found in the appendix.

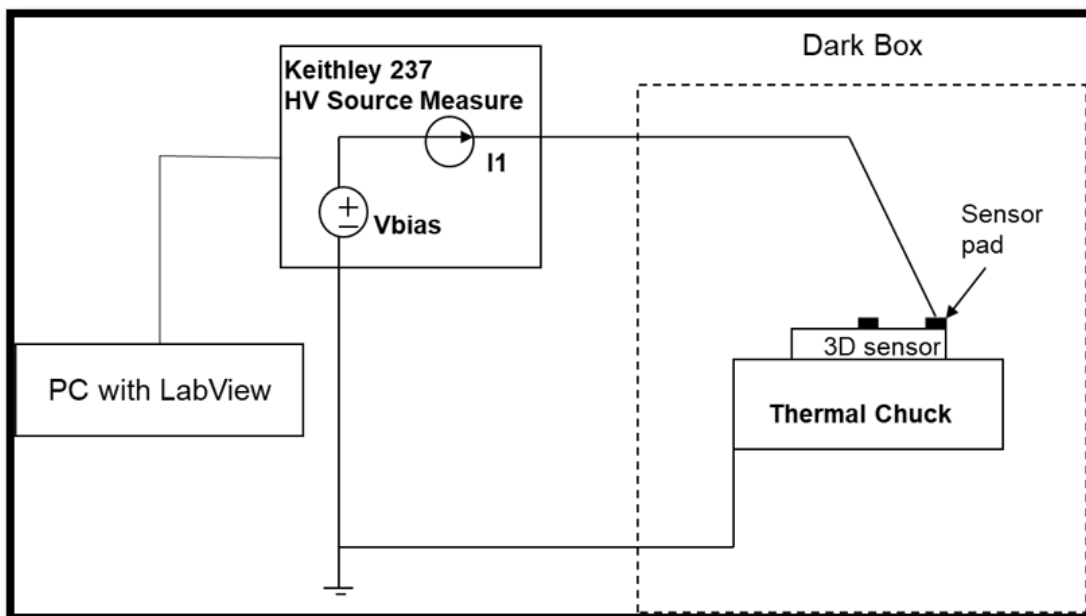


Figure 3.2: A schematic for the breakdown voltage measurement setup.

3.2 Setup for Measurement of Depletion Voltage

As with the breakdown voltage measurements, capacitance measurements are done in a light-tight enclosure using a chuck cooled to $-20\text{ }^{\circ}\text{C}$. The bulk capacitance of the sensor is measured. Fig. 3.3 shows a schematic of the setup used for measuring capacitance. The Keithley 237 Sourcemeter supplies the bias voltage while an HP 4284A LCR meter makes measurements of capacitance. Capacitance is measured by applying a reverse bias voltage to the sensors and sweeping from 0 V to 150 V in 1 V increments. The frequencies used for this measurement are 10 kHz, 100 kHz, and 1 MHz. Three measurements of capacitance are made at each step and the average is recorded. Graphs for the capacitance measurements are found in the appendix.

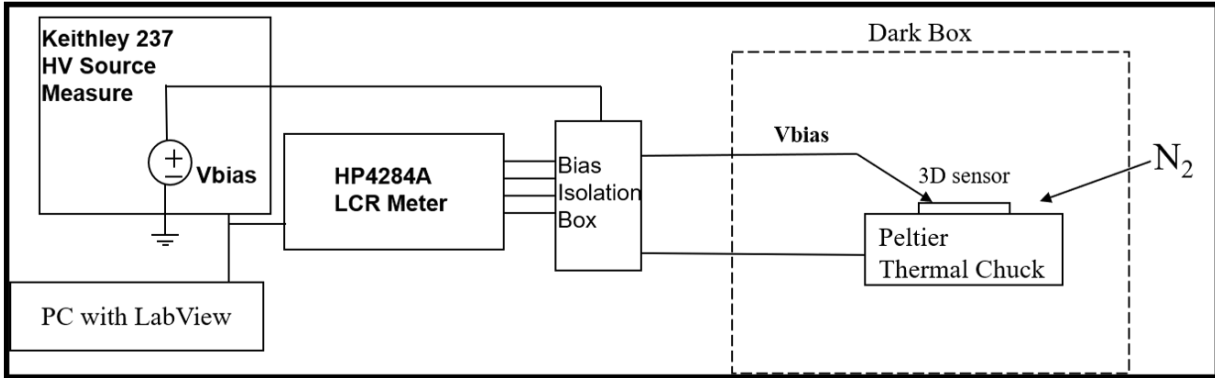


Figure 3.3: A schematic for the depletion voltage measurement setup.

3.3 Setup for Measurement of Charge Collection Efficiency

For this measurement, the sensors are bonded to a test board to read out the signal from a through-going particle. A thin layer of conductive silver epoxy called Loctite Ablestik 2902 is used to attach the sensor to the test board. The silver epoxy is cured at 60 °C for 80 minutes.

The sensor and thermal chuck are again enclosed in a light-tight station. A wire bond is made from the sensor to an isolated lead on the test board. A coaxial cable can be soldered onto the isolated lead. This cable allows for a bias voltage to be applied and the signal to be read out from the sensor. A 1064 nm laser is positioned above the sensor. The laser is pulsed at 10 kHz with a 10 ns pulse width. The 10 ns pulse width is enough to saturate the sensor and create charge carriers throughout the bulk. The frequency of the pulse is long enough to allow the sensor to collect all the charge carriers and deplete the bulk in time for the next pulse. The laser is positioned over the sensor so that most of the active region of the sensor is covered by the laser light. Fig. 3.4 is a photograph of a sensor affixed to a test board.

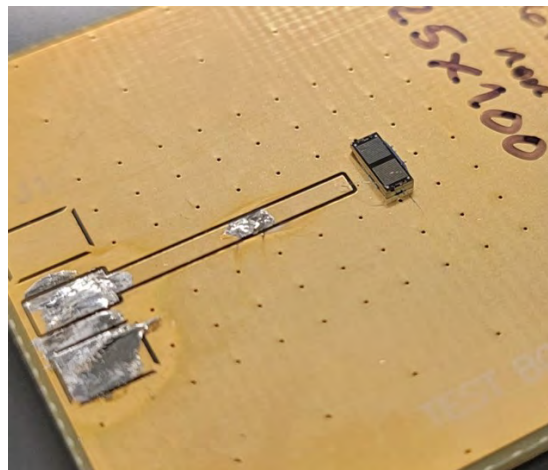
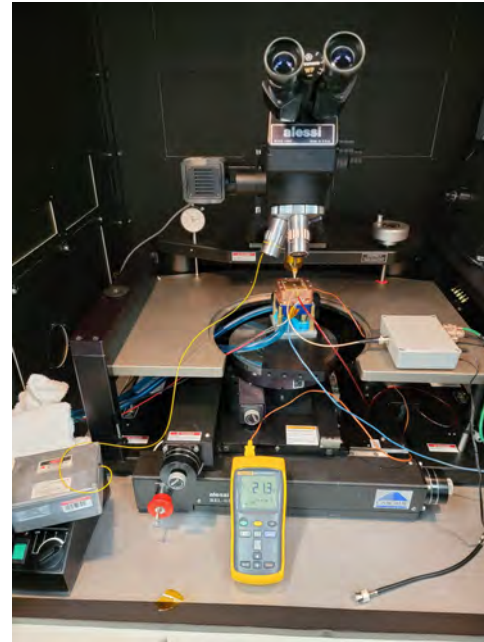
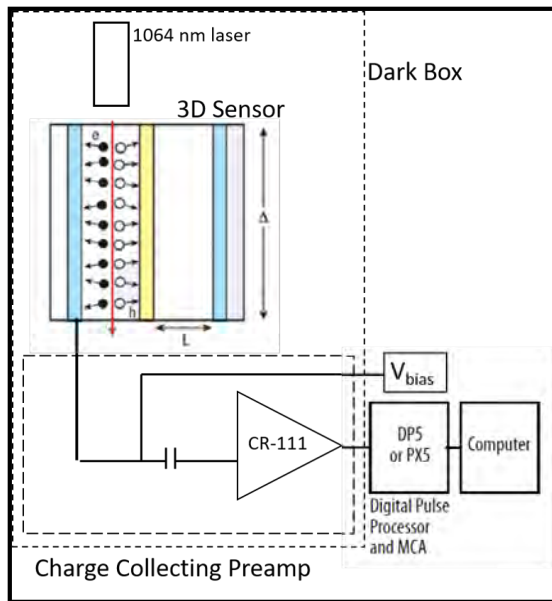


Figure 3.4: This is a close view of a sensor wafer on a test board. A wire bond is made from the contact pad on the surface of the sensor to the test lead on the board. A coaxial cable can be soldered on the test lead to read out the signal and apply a bias voltage (not shown).

The charge carriers travel to the Cremat CR-111 preamplifier. The signal then passes to the Amptek DP5 digital pulse processor and multichannel analyzer (MCA). The DP5 is controlled by software that allows the pulse to be shaped. The MCA creates a histogram of the pulse height, which is proportional to the signal charge from the sensor. Fig. 3.5 shows a schematic and a photograph for the charge collection setup.



(a) A schematic of the setup for charge collection measurements. Part of this figure is reproduced from source [2].

(b) Photograph of the setup for the charge collection measurements.

Figure 3.5

The CR-111 and the DP5 have to be calibrated. The DP5 is calibrated by injecting a known amount of charge and determining the gain conversion. A function generator controls the amount of charge applied to the test input of the CR-111. The function generator generates a set of square waves that increase in amplitude with each test.

The average charge Q is then given by

$$Q = CV$$

where C is the capacitance of the test capacitor and V is the average amplitude of the square wave (in volts.) The MCA software creates a histogram with the channel number corresponding to the pulse height of the digitized signal. The histogram is a Gaussian curve with the peak centered on the channel corresponding to the average charge injected.

After measurements are made for different values of injected charge, a plot is made showing channel number versus injected charge. A linear fit is made to these data. The inverse of the slope of the resulting line is the gain conversion used to determine the amount of charge per MCA channel. Calibration for the laser charge collection efficiency is not necessary as this is a relative measurement of gain. The charge collection gain can be calculated without calibrating the MCA channel to electrons.

To measure charge collection efficiency, a bias voltage is applied while the laser is applied to the sensor. The MCA records the pulse heights on a histogram where the bins are the ADC channels. Fig. 3.6 shows the display of the MCA software during data acquisition. The horizontal axis is the ADC channel and the vertical axis is the counts. The signal is centered around channel 1076 and is well separated from the noise. The noise is effectively filtered by the digital pulse processor and the cutoff is at channel 212. Between channels 212 and 260, the tail end of the noise appears as a small amount and is not filtered. The software displays a reconstruction of the input signal from the preamplifier as a digital oscilloscope inset on the main MCA window. The data are exported to a file and data analysis continues using Origin software.

In Origin, a Gaussian curve is fitted to the data to determine the mean ADC channel and the standard deviation. Fig. 3.7 shows a sample data peak with a Gaussian curve fitted to the data. The mean ADC channel and the standard deviation are recorded for each bias voltage. The mean channel is plotted against the bias voltage, with the statistical uncertainty of the mean ADC channel being representing the standard deviation of the fitted curve. This resulting curve represents the amount of charge collected at specific voltages. The mean ADC channel, which represents the amount of charge collected, should rise until the sensor is fully depleted. In the absence of charge multiplication, it will then plateau until the breakdown voltage is reached. If charge multiplication is present, the charge collected should increase before breakdown voltage is reached.

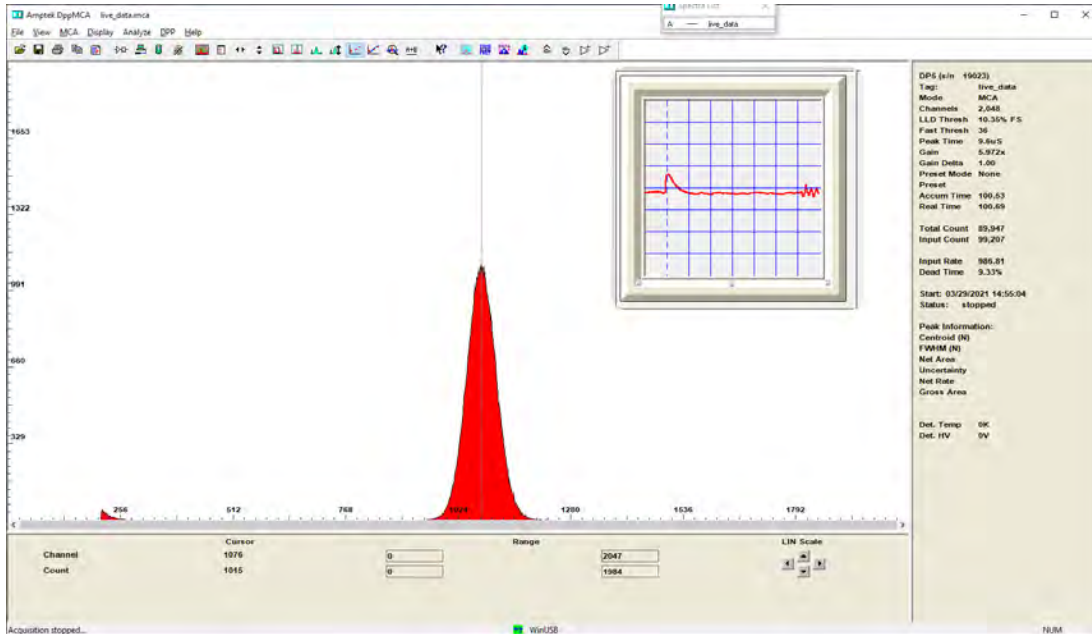


Figure 3.6: Display of MCA data acquisition. The MCA software shows a reconstruction of the input from the preamplifier as a digital oscilloscope inset on the histogram.

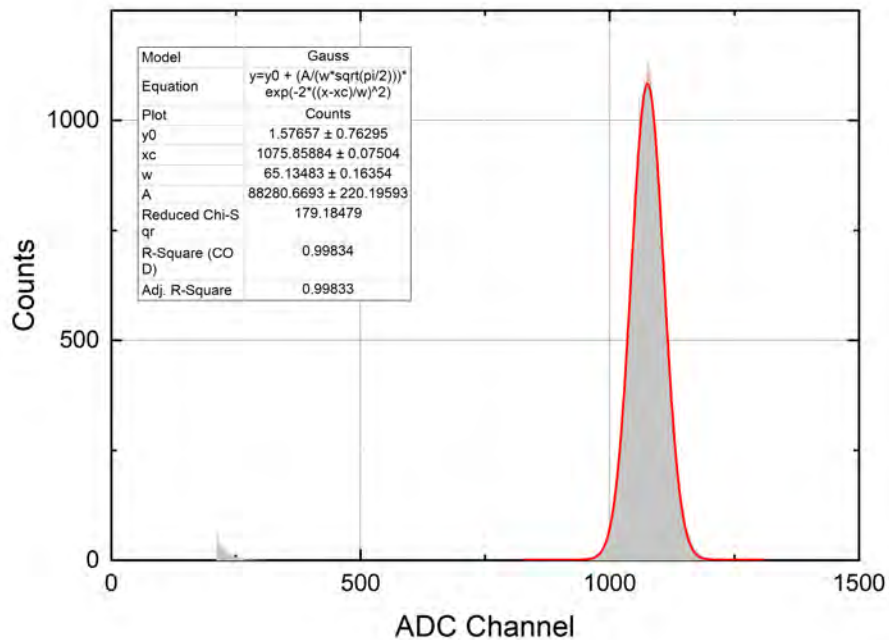


Figure 3.7: Sample data analysis using Origin software. A Gaussian curve is fitted to the data. The mean and the standard deviation are recorded.

4. Results

Irradiation can damage a silicon sensor to the point where it becomes conductive and unable to function as intended. This is the case with a majority of the sensors that were irradiated for this study. Out of the six sensors of cell size $25 \times 25 \mu\text{m}^2$ that were irradiated, only one maintained a breakdown voltage above 40 V. Due to time constraints, this sensor is the only irradiated sensor that is tested for this study because it is the most likely candidate in which to find charge multiplication.

The sensor that was able to be tested was irradiated to a fluence of $3.0 \times 10^{16} \text{ n}_{\text{eq}}/\text{cm}^2$. Its breakdown and depletion voltages were recorded as 127 V and 17 V respectively.

The gain z is calculated using

$$z = \frac{x}{y}$$

where x is the mean ADC channel just below breakdown and y is the mean ADC channel near the depletion voltage. The uncertainty in gain δz is calculated using

$$\frac{\delta z}{z} = \sqrt{\left(\frac{\delta x}{x}\right)^2 + \left(\frac{\delta y}{y}\right)^2}$$

where z is the calculated gain, x and y are the mean ADC channels, and δx and δy are the standard deviations of the fitted Gaussian curves. The irradiated $25 \times 25 \mu\text{m}^2$ sensor shows a gain of 2.0 ± 0.2 . Fig. 4.1 shows a graph with the ADC channel versus the bias voltage.

Three non-irradiated sensors are also measured for depletion and breakdown voltages and charge collection efficiency. Their dimensions are $50 \times 50 \mu\text{m}^2$, $25 \times 25 \mu\text{m}^2$, and $25 \times 100 \mu\text{m}^2$ 1E. The breakdown and depletion voltages for the $50 \times 50 \mu\text{m}^2$ are 145 V and 4 V respectively. Fig. 4.2 shows the charge collection efficiency with the mean ADC channel plotted against the bias voltage. This sensor does not show any evidence of charge multiplication before breakdown.

The breakdown and depletion voltages for the $25 \times 25 \mu\text{m}^2$ non-irradiated sensor are 93 V and 1 V respectively. Fig. 4.3 shows a graph of the charge collection rates for this sensor. The mean ADC channel increases slightly near the breakdown voltage. This sensor shows a gain of 1.3 ± 0.1 .

The sensor with dimensions $25 \times 100 \mu\text{m}^2$ 1E has a breakdown voltage of 153 V and a depletion voltage of 2 V. Fig. 4.4 shows the charge collection rate of this sensor. The gain in the charge collection rate is most likely due to higher charge collection efficiency at higher voltages rather than to charge multiplication.

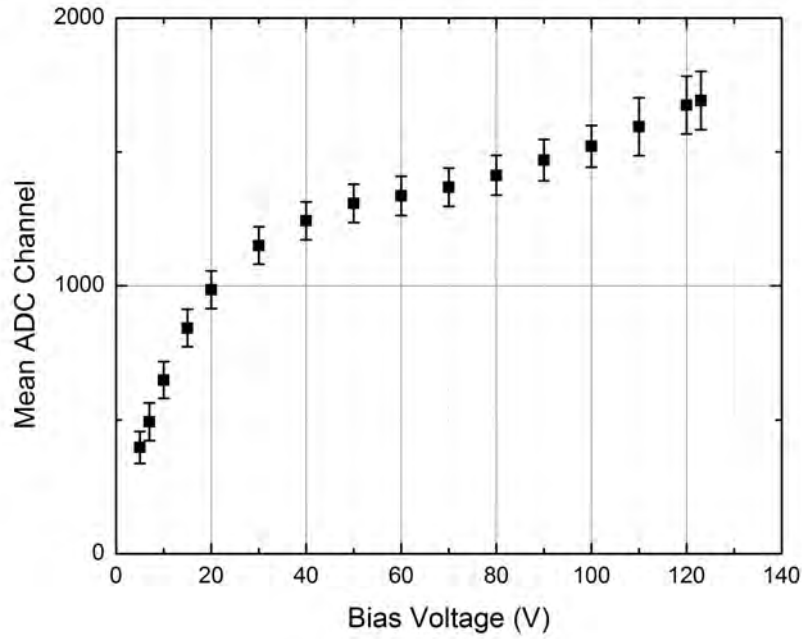


Figure 4.1: Graph showing the mean ADC channel versus bias voltage for the $25 \times 25 \mu\text{m}^2$ sensor irradiated to $3.0 \times 10^{16} \text{ n}_{\text{eq}}/\text{cm}^2$. The amount of charge collected is proportional to the ADC channel.

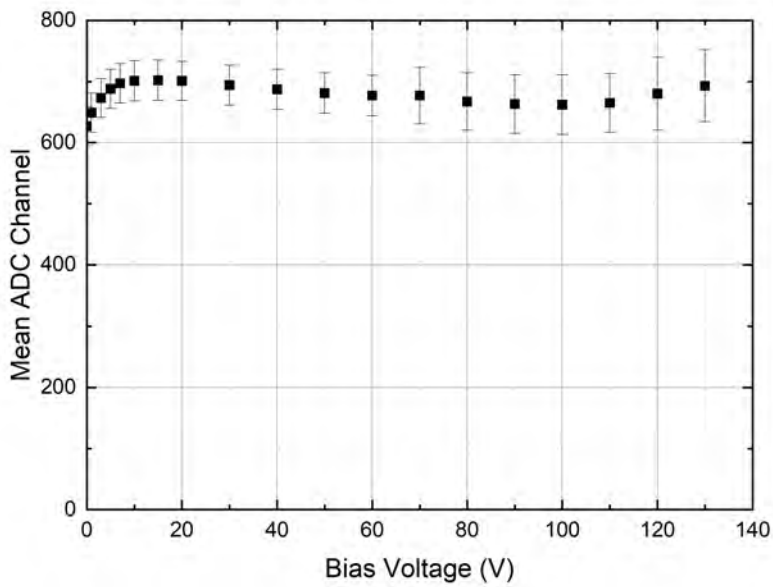


Figure 4.2: A graph of the charge collection efficiency of the non-irradiated sensor with cell dimensions of $50 \times 50 \mu\text{m}^2$. The mean ADC channel does not increase with bias voltage, therefore this sensor does not show any evidence of charge multiplication.

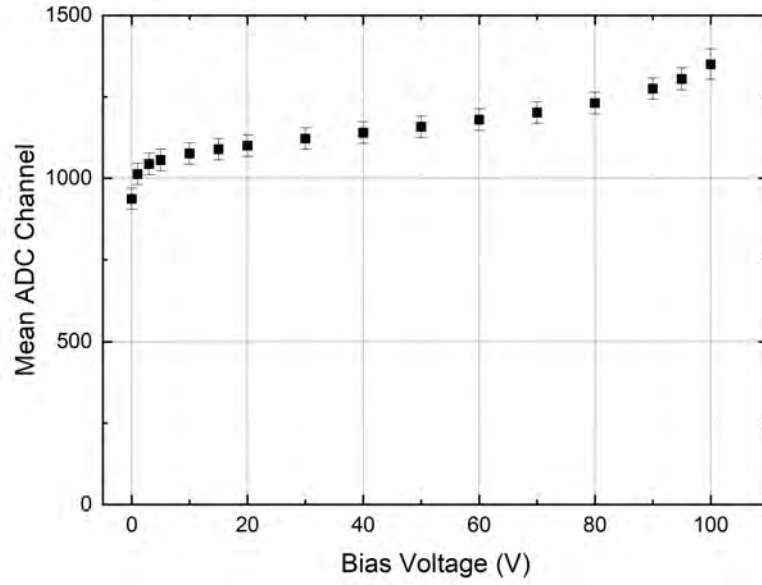


Figure 4.3: A graph of the charge collection efficiency of the non-irradiated sensor with cell dimensions of $25 \times 25 \mu\text{m}^2$. There is a slight increase of mean ADC channel close to breakdown, which would indicate some level of charge multiplication in the sensor.

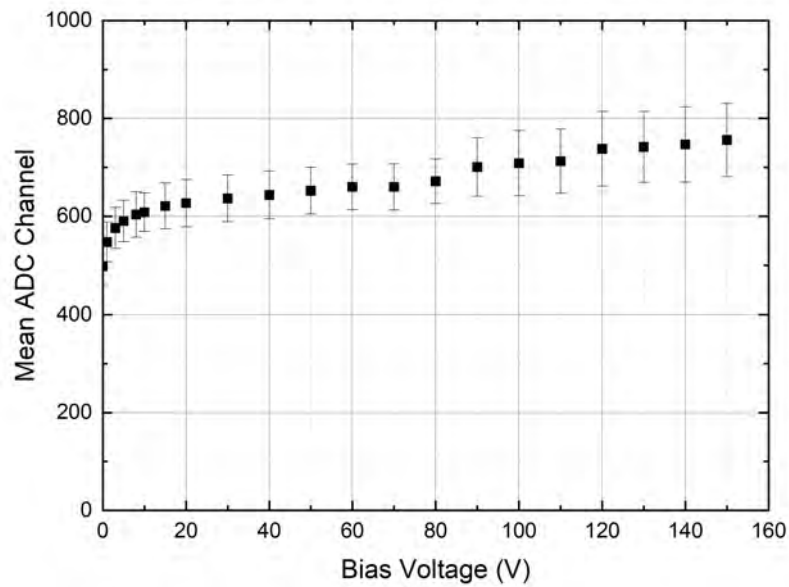


Figure 4.4: A graph of the charge collection rate for the non-irradiated sensor with the cell dimension of $25 \times 100 \mu\text{m}^2$.

5. Conclusion

The results show that the $25 \times 25 \mu\text{m}^2$ geometry of 3D silicon sensors is conducive to controlled charge multiplication, even at proton fluences up to $3.0 \times 10^{16} \text{ neq/cm}^2$. Charge multiplication in these sensors is evident with or without exposure to proton radiation. This suggests that the small-pitch geometry exceeds the critical electric field of 180 kV/cm mentioned in section 2.4 which is a condition for controlled charge multiplication to occur.

The method of collecting charge with a laser is important as it validates the assembly of the sensor on the test board, the preamplifier setup, the digital pulse processor, and the software working together to measure charge collection rates. The next step for this research is to use a ^{90}Sr β^- source as the stimulant to the sensor. My suggested recommendations would be to increase the gain of the signal by decreasing the capacitance of the feedback capacitor in the preamplifier, and decreasing the noise by taking measurements at or below -30°C .

References

- [1] Gian-Franco Dalla Betta. 3D Silicon Detectors. In *Proceedings of INFN Workshop on Future Detectors for HL-LHC — PoS(IFD2014)*, volume 219, page 013, 2015. [Cited on page 7]
- [2] Cinzia Da Via et al. 3D silicon sensors: Design, large area production and quality assurance for the ATLAS IBL pixel detector upgrade. *Nuclear Instruments and Methods*, 694:321–330, 2012. [Cited on page 16]
- [3] Francesco Moscatelli et al. Combined bulk and surface radiation damage effects at very high fluences in silicon detectors: Measurements and TCAD simulations. *IEEE Transactions on Nuclear Science*, 63:2716–2733, 2016. [Cited on page 6]
- [4] Aiden K. Grummer. *A Search for New Physics in $B_{(s)} \rightarrow \mu^+ \mu^-$ Decays Using Multivariate Data Analysis, and Development of Particle Detection Technology with Silicon Pixel Detectors*. Ph.D. dissertation, The University of New Mexico, 2021. [Cited on page 12]
- [5] Esma Mobs. The CERN accelerator complex - 2019. <https://cds.cern.ch/record/2684277>, 2019. Accessed 2021-02-26. [Cited on page 2]
- [6] Michael Moll. Displacement damage in silicon detectors for high energy physics. *IEEE Transactions on Nuclear Science*, 65:1561–1582, 2018. [Cited on page 6]
- [7] Donald A. Neamen. *Semiconductor Physics and Devices*. McGraw-Hill, 2012. [Cited on page 5]
- [8] Anna Peisert. Silicon microstrip detectors. *Instrumentation In High Energy Physics. Series: Advanced Series on Directions in High Energy Physics*, 9:1–79, June 1992. [Cited on page 9]
- [9] Joao Pequeno. Computer generated image of the whole ATLAS detector. <https://cds.cern.ch/record/1095924/>, 2008. Accessed 2021-02-26. [Cited on page 3]
- [10] Sally Seidel. Silicon strip and pixel detectors for particle physics experiments. *Physics Reports*, 828:1–34, 2019. [Cited on page 8]
- [11] Michael Shur. 6 - semiconductors. In Wai-Kai Chen, editor, *The Electrical Engineering Handbook*, pages 153–162. Academic Press, Burlington, 2005. [Cited on page 9]
- [12] Helmuth Spieler. Introduction to radiation detectors and electronics. https://www-physics.lbl.gov/~spieler/physics_198_notes_1999/PDF/V-3-Resolution-3.pdf, 1999. Accessed 2021-02-13. [Cited on page 12]

- [13] Helmuth Spieler. *Semiconductor Detector Systems*. Oxford University Press, 2011. [Cited on pages 6 and 11]
- [14] Kevin Stenson and Achintya Rao. Reconstructing a multitude of particle tracks within CMS. <https://cms.cern/news/reconstructing-multitude-particle-tracks-within-cms>, 2021. Accessed 2021-02-13. [Cited on page 1]
- [15] Ben Streetman and Sanjay Banerjee. *Solid State Electronic Devices*. Pearson, 2006. [Cited on page 10]
- [16] Christine Sutton. Particle accelerator. <https://www.britannica.com/technology/particle-accelerator>, 2021. Accessed 2021-02-13. [Cited on page 1]
- [17] S. M. Sze and Kwok K. Ng. *Physics of Semiconductor Devices*. John Wiley and Sons, 2007. [Cited on page 10]
- [18] Norbert Wermes. Trends in pixel detectors: tracking and imaging. *IEEE Transactions on Nuclear Science*, 51(3):1006–1015, 2004. [Cited on page 7]

Appendix

This appendix includes the current versus voltage (IV) and capacitance versus voltage (CV) characteristic curves for the devices reported in this article.

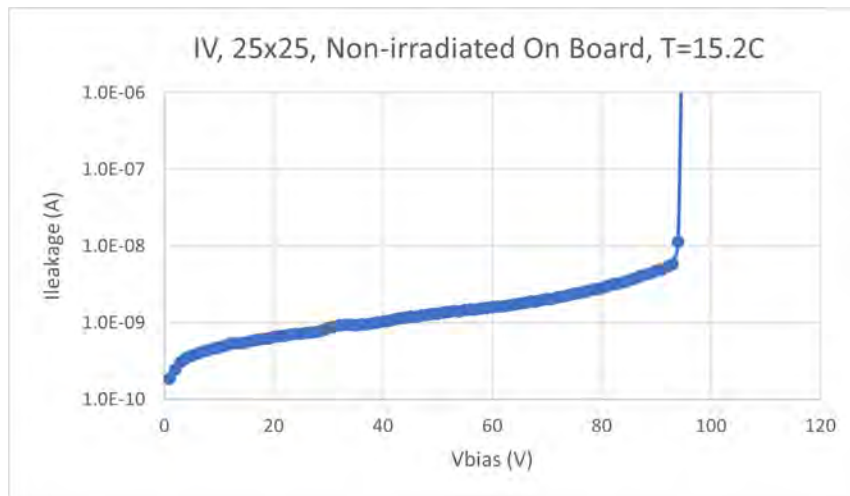


Figure 5.1: Current versus voltage graph for the non-irradiated sensor with a cell size of $25 \times 25 \mu\text{m}^2$.

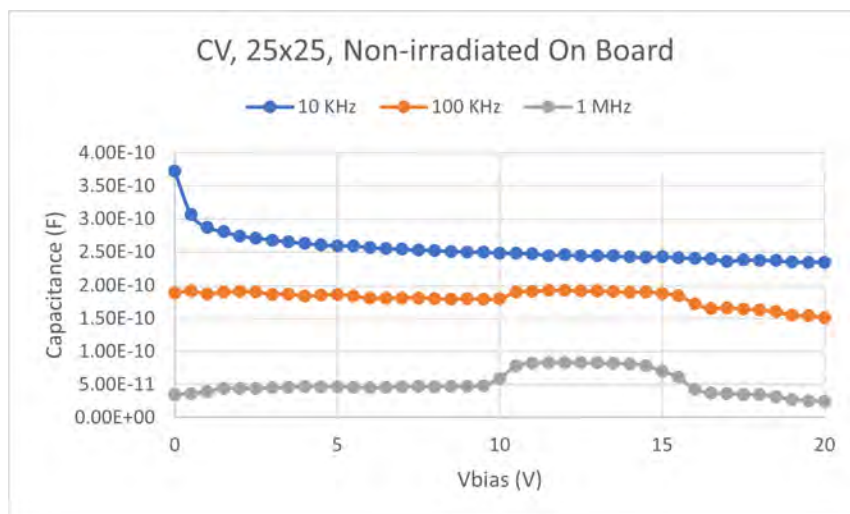


Figure 5.2: Capacitance versus voltage graph for the non-irradiated sensor with a cell size of $25 \times 25 \mu\text{m}^2$.

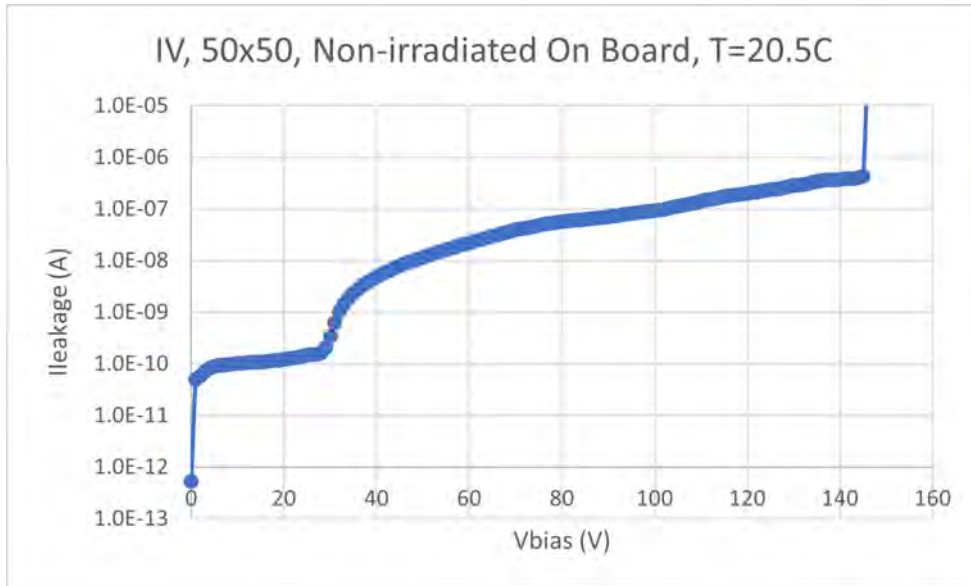


Figure 5.3: Current versus voltage graph for the non-irradiated sensor with a cell size of $50 \times 50 \mu\text{m}^2$.

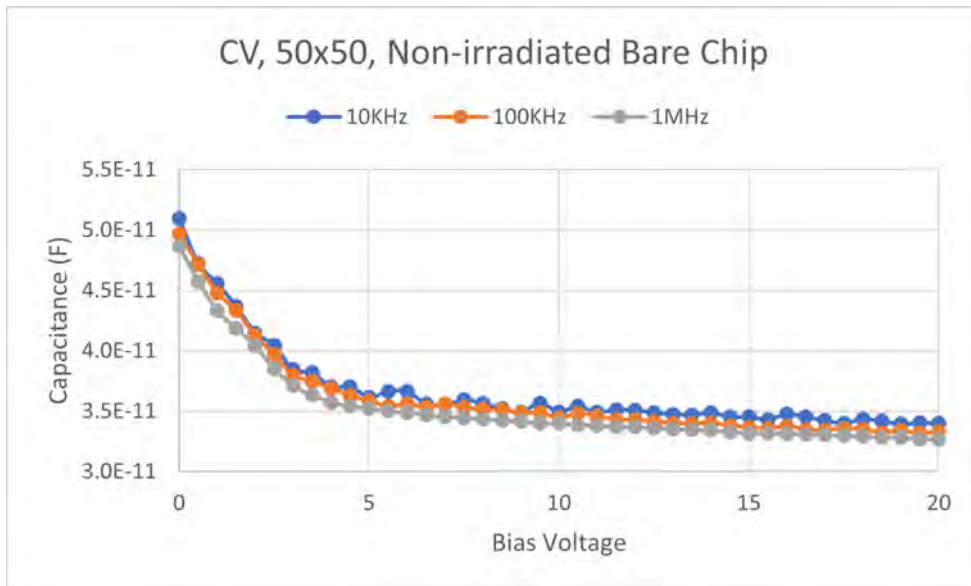


Figure 5.4: Capacitance versus voltage graph for the non-irradiated sensor with a cell size of $50 \times 50 \mu\text{m}^2$.

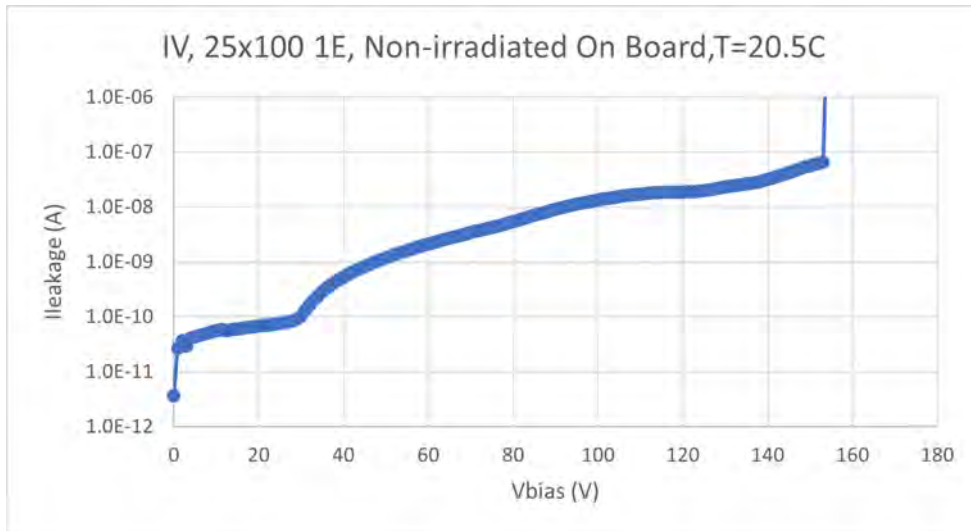


Figure 5.5: Current versus voltage graph for the non-irradiated sensor with a cell size of $25 \times 100 \mu\text{m}^2$ 1E.

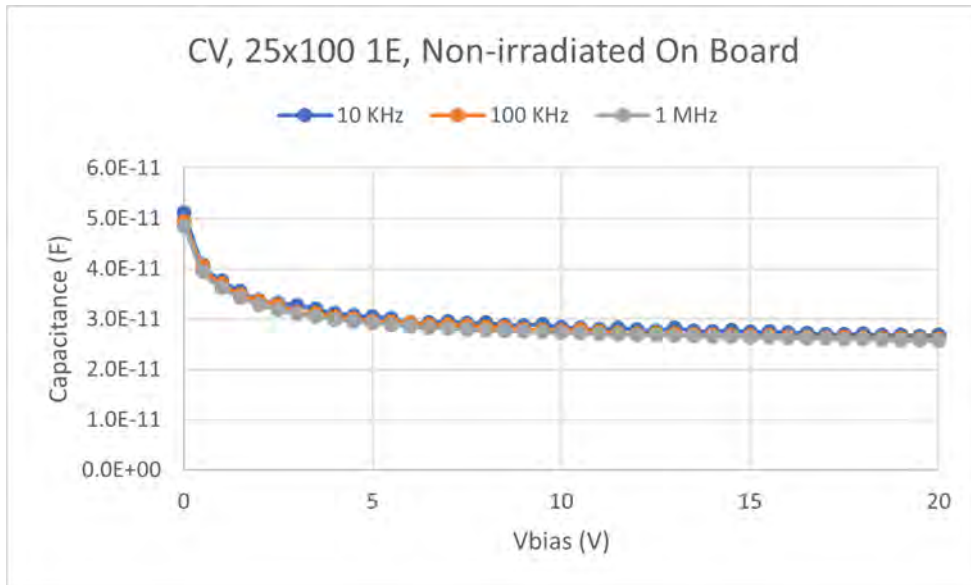


Figure 5.6: Capacitance versus voltage graph for the non-irradiated sensor with a cell size of $25 \times 100 \mu\text{m}^2$ 1E.

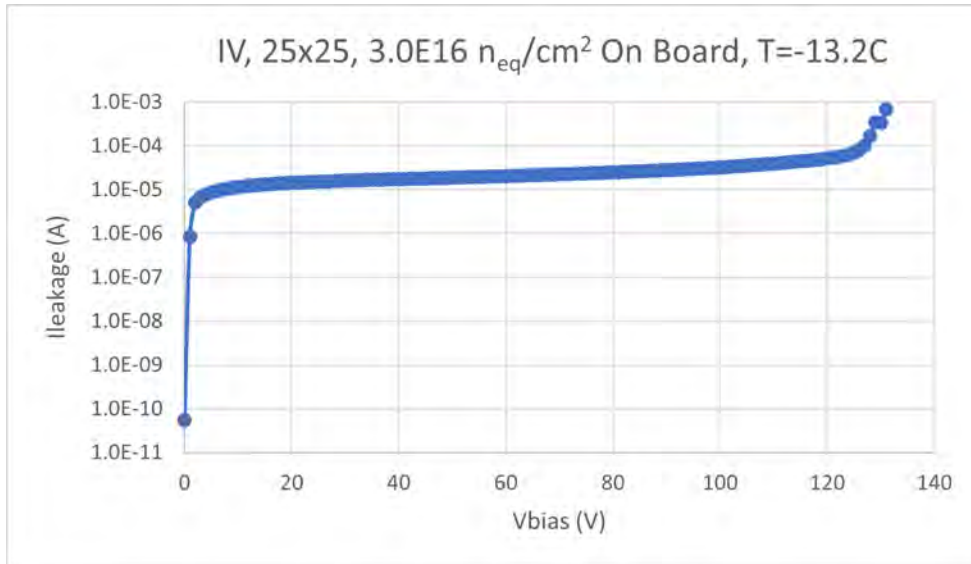


Figure 5.7: Current versus voltage graph for the sensor irradiated to a fluence of 3.0×10^{16} neq/cm² with a cell size of $25 \times 25 \mu\text{m}^2$.

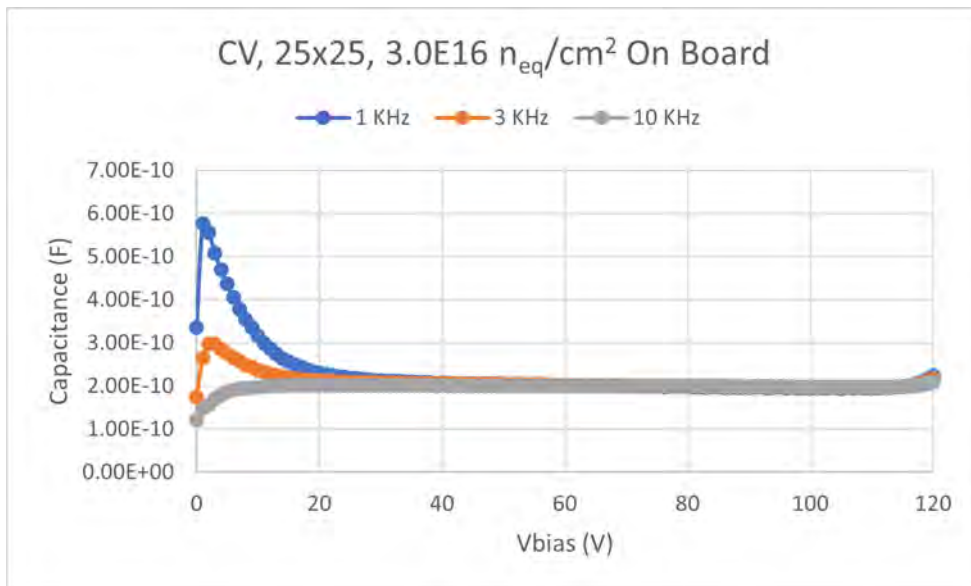


Figure 5.8: Capacitance versus voltage graph for the sensor irradiated to a fluence of 3.0×10^{16} neq/cm² with a cell size of $25 \times 25 \mu\text{m}^2$.